# Chapter 3

# Reliability Assessment of Wind Integrated Power System

## 3.1 Introduction

The thesis work has been expanded in this chapter by evaluating the dependability of an DFIG-based WIPS. The test system used in this research was purposefully subjected to natural lightning impulses and 3-phase faults. As a result, the natural LI voltage and currents are produced, and the LI voltage is regarded a significant cause of system failure, and is used to evaluate the reliability assessment of the test system. However, an identification method was used in the literature to solve the influence of LI phenomena [95], and it was also discovered that the generation of natural lightning phenomena is critical for the testing of devices such as surge arresters, power transformers, and so on.

Furthermore, reliability and cost assessments for High Voltage Direct Current interconnectors for renewable energy integration were performed in [185, 186], and reliability assessment of microgrid architecture was analysed in [187]. For the outage of the 230 kV transmission lines, an Monte-Carlo-based study was conducted, and a probabilistic approach based on the MC technique was used to assess the shielding failure flashover rate and return flashover rate of 230 kV overhead lines [20]. In [188], a quantitative technique for evaluating failure probability was presented, and it was used to estimate the failure probability of two 230 kV transformers, indicating power equipment failure trends. The failure trend is helpful in determining the power equipment and integrated power system's remaining useful life and dependability [189, 190].

The researchers have highlighted the effects of the LI voltage on various HVDC and HVAC

power systems, according to the literature study conducted in Chapter 2. The existing literature, on the other hand, is unable to explain the following key aspects.

- By studying actual analogous circuits, the creation of LI overvoltage and overcurrent is possible.
- Impact study of LI voltage and current phenomena on an DFIG-based WIPS.
- Comparative analysis between 3-phase fault and impulse voltage fault for DFIG-based WIPS.
- Assessment of the reliability of DFIG-based WIPS using impulse voltage as the primary cause of system and/or equipment failure.

Given the aforementioned shortcomings, the chapter's major contributions are as follows, which have been contrasted in Table 2.4. The flow chart in Figure 3.1 depicts the research effort completed in this chapter.

1. Firstly, the proposed PSO algorithm has been compared with [22].
2. Realistic equivalent circuits are used to produce impulse voltage, impulse current, and Rectangular Pulse Current Generation (RPCG) waveforms. Equivalent circuits are made up of a resistor, an inductor, and a capacitor, with the inductor and resistor being distinguished by their tiny internal resistance and inductance, respectively.
3. The impact of LIV on the system parameters of DFIG-based WECS is observed.
4. The system is subjected to a three-phase fault, and the findings are compared to those obtained in contribution 3.
5. To obtain optimum values of sixth order transfer function gains, including $kp$ and $ki$ for improved output responses, the PSO method is used.
6. The MC technique is used to assess the reliability of the WIPS system.

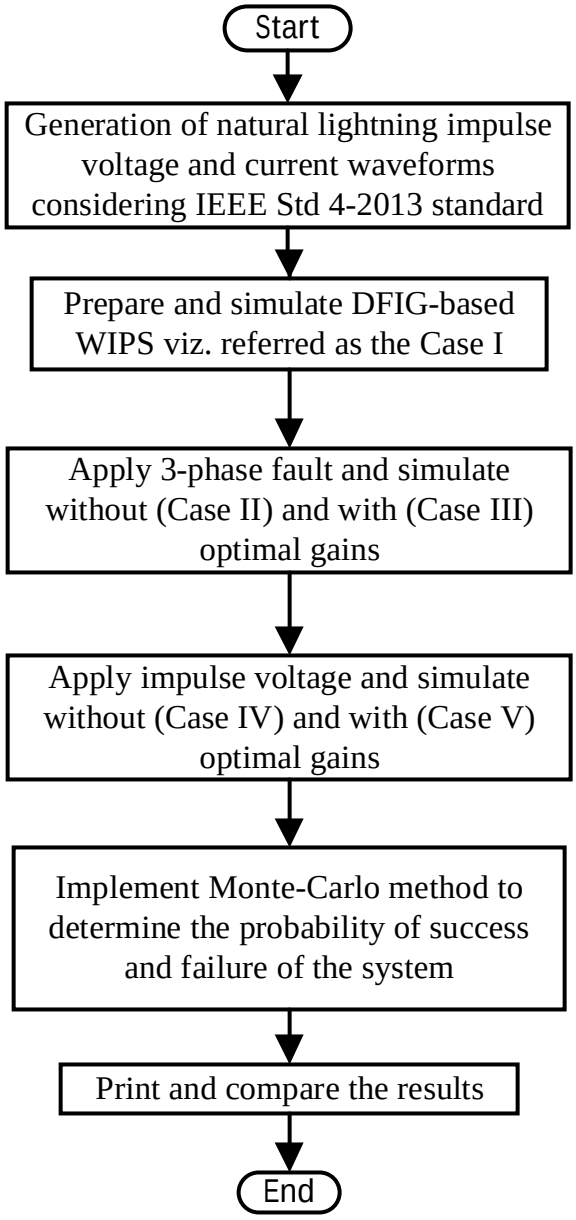


Figure 3.1: Flow chart of research work performed in this chapter.

## 3.2 Problem Statement

According to the literature, when the effect of lightning impulse and 3-phase fault is not accessible, research and analysis were conducted using DFIG-based WIPS characteristics. Furthermore, the system's reliability assessment has not been performed in the face of an LIV strike. As a result, it is critical to investigate the behaviour of the system's characteristics when natural lightning and a three-phase fault are used. In this respect, the focus of the current chapter is on the effects of the aforementioned faults on system parameters such as active power, reactive

power, rotor-speed ($\omega_r$), and dc-link voltage ($V_{dc}$). Also, performed the reliability assessment considering the impulse voltage as a major cause of system failure.

Furthermore, the lightning envelopes are generated by using the equivalent electrical circuits. After the generation of impulse voltage and current waveforms,[1] the impacts of these impulse waveforms on WIPS is analyzed.[2] Figure 3.2 illustrates a schematic layout of DFIG-based WIPS integrated into the main grid with a configuration of the rotor and grid side converters, where $C$ is the ripple-free DC-link capacitor.

The chapter has been expanded by implementing a sixth order transfer function ($TF$) model of WTG, as given in Equation (3.1) adapted from [85, 96], for computing optimal proportional ($k_p$) and integral ($k_i$) gains values using the PSO technique [191, 192]. The output responses show that after obtaining the optimal gain values of WTG's transfer function, the system's performance characteristics significantly improved. Finally, when failures occur in VSC due to a lightning strike, the MC technique has been developed to evaluate the system's reliability.

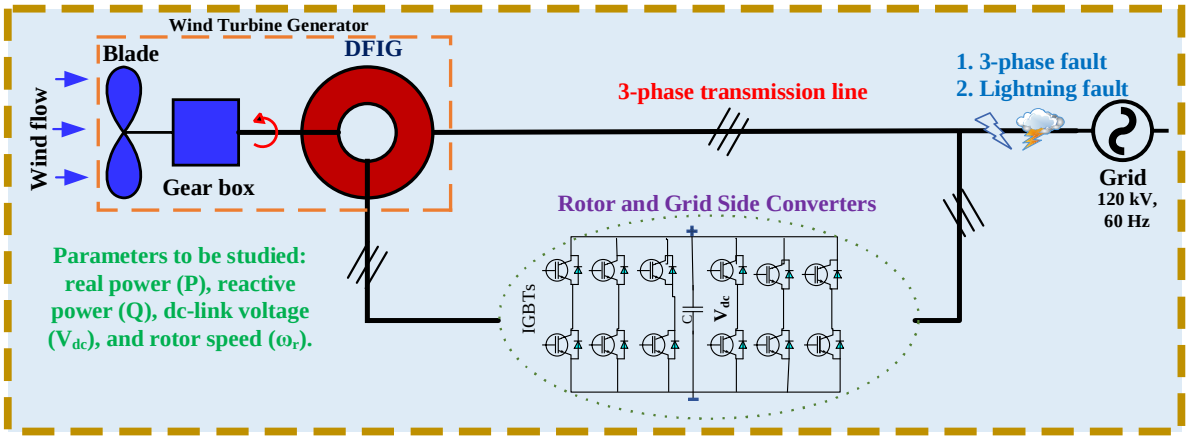


Figure 3.2: Wind integrated power system with Rotor and Grid Side Converters.

$$TF = \frac{N_1 S^6 - N_2 S^5 - N_3 S^4 + N_4 S^3 + N_5 S^2 + N_6 S + N_7}{S^6 + D_1 S^5 + D_2 S^4 + D_3 S^3 + D_4 S^2 + D_5 S + D_6} \tag{3.1}$$

Where

- $N_1 = 0.000324$, $N_2 = 1.75$, $N_3 = 2366$, $N_4 = 7.9 \times 10^6$, $N_5 = 7.5 \times 10^9$, $N_6 = 5 \times 10^{12}$, $N_7 = 2.18 \times 10^{14}$

[1] detail of waveform generation can be found later this chapter

[2] refer to Figure 3.2

- $D_1$ = 2340, $D_2$ = $8.67 \times 10^6$, $D_3$ = $4.79 \times 10^9$, $D_4$ = $2.7 \times 10^{12}$, $D_5$ = $1.27 \times 10^{14}$, $D_6$ = $9.6 \times 10^{14}$

As per Equation (3.2), the DFIG performance usually depends on the gain levels ($kp$ and $ki$) of the Proportional Integral (PI) controller. The Integral Square Error has been considered as an objective function that must be minimized for a particular transfer function at optimal values of gains.

$$\text{Integral Square Error} = \int_0^\infty e^2(t)dt \tag{3.2}$$

Where e(t) is the error function of time.

## 3.3 Lightning Impulse Voltage and Current Generation

Table 3.1 describes the timing and tolerance parameters of standard impulse waves, which are adopted from IEEE Std 4-2013 [193]. This chapter then goes on to discuss several kinds of impulse voltage and current generating circuits that are often used to produce standard impulse voltage and current (as listed in Table 3.1). These impulse waves have a front (rise) period of the order of 0.5 to 10 $\mu$s and a tail (decay) duration (to 50% of the peak value) of the order of 30 to 200 $\mu$s, according to the tests described in IEEE Std 4-2013. Three different lightning waveforms are created. The following subsections provide a description of various waveforms [194].

Table 3.1: Parameters of time with tolerances for some standard impulse waves

| **Type of waveform** | $T_f(\mu s)$ | $T_t(\mu s)$ |
|---|---|---|
| LI voltage | $1.2 \pm 30\%$ | $50 \pm 20\%$ |
| Switching impulse (SI) voltage | $250 \pm 30\%$ | $2500 \pm 20\%$ |
| ” | $100 \pm 30\%$ | $1500 \pm 30\%$ |
| Impulse Current-Type I | $4.0 \pm 10\%$ | $10.0 \pm 10\%$ |
| Impulse Current-Type II | $8.0 \pm 10\%$ | $20.0 \pm 10\%$ |
| Rectangular pulse Current | **Peak duration** ($\mu$s) | **Total duration** ($\mu$s) |
| | 500, 1000, or 2000 | 2000 to 3200 |

### 3.3.1 Impulse Voltage Generation

In the real world, resistance has a tiny internal inductance, and the inductance provides a small internal reactance, leading to various outputs. The inductance $L_f$ is the internal inductance provided by the front resistance $R_f$, which is responsible for the lightning impulse overshoot, which must be kept below 5% [195]. Similarly, the internal inductance provided by the impulse circuit's tail resistance $R_t$ is $L_t$. To achieve a more realistic waveform, these inductances have been incorporated into the equivalent circuit. The impulse voltage is defined as a double exponential waveform featuring 1.2 $\mu$s of rise time and 50 $\mu$s of tail time, as per IEEE Std 4-2013. The necessary procedures are used to produce the required standard impulse voltage.

- Step 1: $V$ is applied at t = 0s with Spark Gap (SG) is not triggered.
- Step 2: The $C_g$ gets charged to $V$ through $R_s$ for time 0.04s.
- Step 3: The SG is triggered at 0.04s and $C_g$ gets discharged through the load.

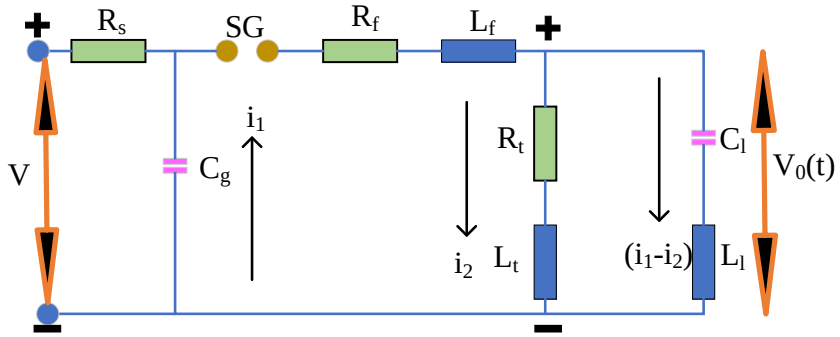


Figure 3.3: Equivalent circuit of impulse voltage generation.

A standard impulse voltage is represented as a double exponential wave as defined in Equation (3.6), which can be derived by using Equations (3.3), (3.4), and (3.5). It is assumed that the small internal inductances $L_f$, $L_t$, and $L_l$ of circuit parameters $R_f$, $R_t$, and $C_l$, respectively, have been ignored in the calculation.

$$V_0(t) = \frac{1}{C_l}\int (i_1 - i_2)dt \tag{3.3}$$

$$\frac{1}{C_g}\int i_1 dt + R_f i_1 + \frac{1}{C_l}\int (i_1 - i_2)dt = 0 \tag{3.4}$$

$$V_0(t) = i_2 R_t \tag{3.5}$$

$$V_0(t) = V_p[exp(-\alpha t) - exp(-\beta t)] \tag{3.6}$$

Where

- $V_p$ is the output peak voltage
- $\alpha$ and $\beta$ are constants of inverse microsecond values

An equivalent Impulse Voltage Generation circuit is shown in Figure 3.3. In this circuit,

- $V$ is the charging voltage
- $R_s$ is the charging resistor
- $C_g$ is generator capacitance
- $i_1$ and $i_2$ are the branch currents in $C_g$ and $R_t$, respectively
- $R_f$ is front resistance
- $R_t$ is tail resistance
- $C_l$ is load capacitance
- $L_f$, $L_t$, and $L_l$ are the front, tail, and load inductance (internal inductance of $R_f$, $R_t$, and $C_l$, respectively)

A standard LI voltage with 1.2 $\mu$s of rise time and 50 $\mu$s of tail time can be generated with the help of a given circuit. The front (rise) $(T_f)$ and tail time $(T_t)$ are empirically defined as given in Equations (3.7a) and (3.7b).

$$T_f = 3 \times R_f \frac{C_g \times C_l}{C_g + C_l} \tag{3.7a}$$

$$T_t = 0.7(R_f + R_t)(C_g + C_l) \tag{3.7b}$$

### 3.3.2 Lightning Current Generation

The series resistance, $R$ represents the internal resistance offered by the inductance, $L$ in the circuit. Similarly, internal inductance, $L_l$ offered by the dynamic load resistance, $R_l$ of the impulse circuit. These internal inductance and resistance are incorporated in the equivalent circuit to provide a more realistic results. As per 'IEEE Std 4-2013', the impulse current has been described as a exponential waveform, having 4 $\mu$s or 8 $\mu$s of rise time and 10 $\mu$s or 20 $\mu$s of tail time. Therefore, an equivalent circuit for the generation of naturally occurred lightning impulse current with capacitive storage is shown in Figure 3.4. Where

- $V$ is charging voltage
- $R_s$ is charging resistance
- $C_g$ is generator capacitance
- $R$ is internal loop resistance offered by $L$
- $L$ is loop inductance
- $R_l$ is load resistance
- $L_l$ is internal load inductance offered by $R_l$
- $I(t)$ is the output impulse current

The impulse current of required shape is generated by using the following steps.

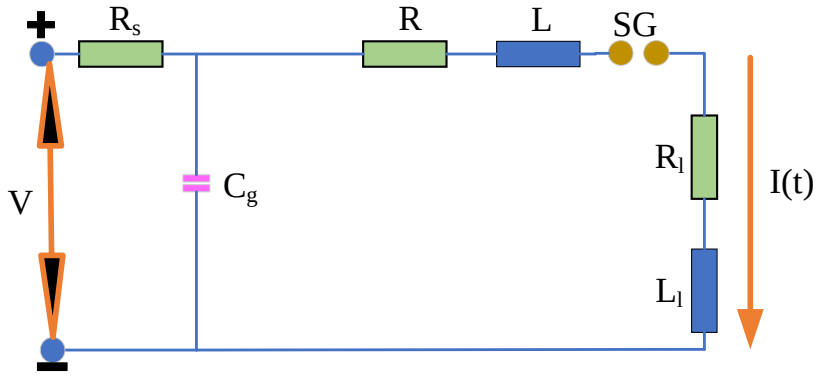


Figure 3.4: Equivalent circuit of impulse current generation.

- Step 1: $V$ is applied at t = 0 s with SG is not triggered.

- Step 2: The $C_g$ gets charged to $V$ through $R_s$ for time 0.04 s.
- Step 3: The SG is triggered at 0.04 s and $C_g$ gets discharged through the inductive load.

A bank of capacitors linked in parallel is charged to a predetermined value and discharged via a series R-L circuit for generating high impulse currents, as illustrated in Figure 3.4. $C_g$ is a bank of capacitors linked in parallel and charged to a voltage of up to 100 kV from a DC source. The dynamic resistance of the test item is represented by $R_l$, which is referred as a load. An air-cored high-current inductor, typically a spiral tube with a few turns, is denoted as $L$. The current may be calculated as if the capacitor is charged to a voltage $V$ and discharged when the spark gap is activated. Equation (3.9) is a second order differential equation that has been created and transformed to Laplace form. Equation (3.10) describes current in the overdamped state D $> 0$, which may be obtained using the circuit Equation (3.8).

$$\frac{1}{C_g}\int I(t)dt + RI(t) + L\frac{dI(t)}{dt} = 0 \tag{3.8}$$

$$s^2 + \frac{R}{L}s + \frac{1}{LC_g} = 0 \tag{3.9}$$

$$I(t) = I[exp(-\alpha t) - exp(-\beta t)] \tag{3.10}$$

Where $I = \frac{V}{pL}$, $p = (\alpha - \beta)$, $V$ is the charging voltage, $L$ is the circuit inductance, $\alpha$ and $\beta$ are the roots of the equation.

For underdamped condition D $< 0$, current is described as follows.

$$I(t) = I[exp(-at)sin\frac{\sqrt{-D}}{2}t] \tag{3.11}$$

Where $I = \frac{V}{qL}$, $q = \frac{\sqrt{-D}}{2}$, $a = \frac{R}{2L}$, discriminant $D = (\frac{R}{L})^2 - \frac{4}{LC_g}$.

The duration of the peak of a rectangular impulse current ($T_d$) and the overall duration of a rectangular impulse current ($T_t$) have been used to define the rectangular pulse current. The period when the current is higher than 90% of its peak value is called $T_d$, and the time when the current is greater than 10% of its peak value is called $T_t$. Table 3.1 shows the values of $T_d$ and $T_t$ according to the 'IEEE Std 4-2013'. The RPCG is essential when a high-energy current pulse is discharged into the system. $E = V \times I_a \times T_d$, where $V$ represents the system voltage, $I$ represents the peak current, and $T_d$ represents the length of the rectangular current pulse. Studies are conducted out using an artificial transmission line model, as shown in Figure 3.5,

which includes an internal load inductance for more realistic findings, in order to achieve the naturally occurring rectangular current pulse.

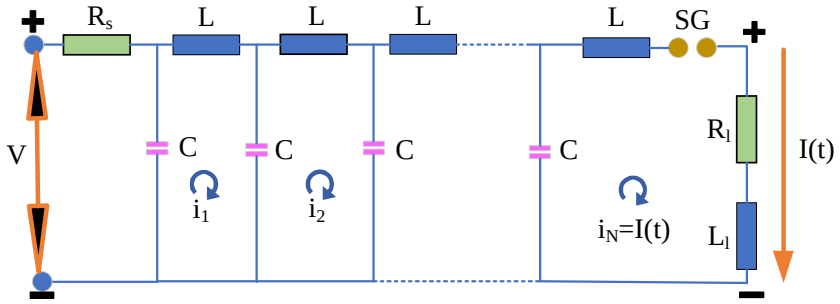


Figure 3.5: Equivalent circuit of rectangular pulse current generation.

The inductance ($L$) and capacitance ($C$) per metre length of a ladder network serve as portions of the transmission line utilised to produce a rectangular current pulse. The loop 1, 2,..., N currents are represented by $i_1$, $i_2$,....., $i_N$ in this circuit. The line charges slowly due to the existence of series and shunt inductance and capacitance, respectively. When the voltage wave advances at the same rate as the line current delivers charge to the wave-front, a voltage change occurs. The current wave moves at the same rate as the voltage wave, which appears at the wave-front over a small length of conductor. It begins the current in the inductance's corresponding line segment. As a result, current and voltage waves must travel alongside each other along the line. Equations (3.12) - (3.16) define the mathematical equations for the present pulse.

$$\tau = \sqrt{LC} \tag{3.12}$$

$$Z_c = \sqrt{\frac{L}{C}} \tag{3.13}$$

$$I = \frac{V}{2R_l} \tag{3.14}$$

$$T = 2(N-1)\sqrt{LC} \tag{3.15}$$

$$\nu = \frac{1}{\sqrt{LC}} \tag{3.16}$$

Where

- $\tau$ is time to travel of a pulse in one meter section length
- $Z_c$ is characteristic impedance
- $I$ is current pulse
- T is current pulse duration
- $\nu$ is propagation velocity
- $R_l$ is load resistance
- $L_l$ is internal inductance of load resistance
- $N$ is number of $LC$ sections and it has typical value between 6 to 9 for proper generation of rectangular current pulse.

## 3.4 Optimization Technique and Monte-Carlo Method

The PSO technique is used to find the best values for the DFIG controller gains, such as $k_p$ and $k_i$, while the Monte-Carlo simulation method is used to evaluate the reliability of the VSC system under investigation. The PSO and MC techniques are described in depth in the subsequent sections of this chapter.

### 3.4.1 Particle Swarm Optimization

Since 1995, PSO has been in use as a new progressive computational method. Reactive power dispatch, generation scheduling, renewable source integrated power systems, and cost analysis all use this technique. The candidate solution is improved repeatedly in this technique under any specified constraint. Figure 3.6 illustrates the PSO algorithm. The fitness function is used to calculate the gain of the PI controller. The best fit solution is then obtained by including this function into the sixth order DFIG model, as generated by Equation (3.1).

It's a swarm behavior-based optimization technique that uses fish schooling or bird flocking to keep track of the particles and find the optimum global solutions. The birds' flocking behaviour is ascribed to the operating concept of PSO [196]. Population size = 30, maximum iteration = 50, maximum inertia weight (wMax) = 0.9, minimum inertia weight (wMin) = 0.2, constant ($c_1$) = 2, constant ($c_2$) = 2 are the PSO parameters examined in this chapter [197].

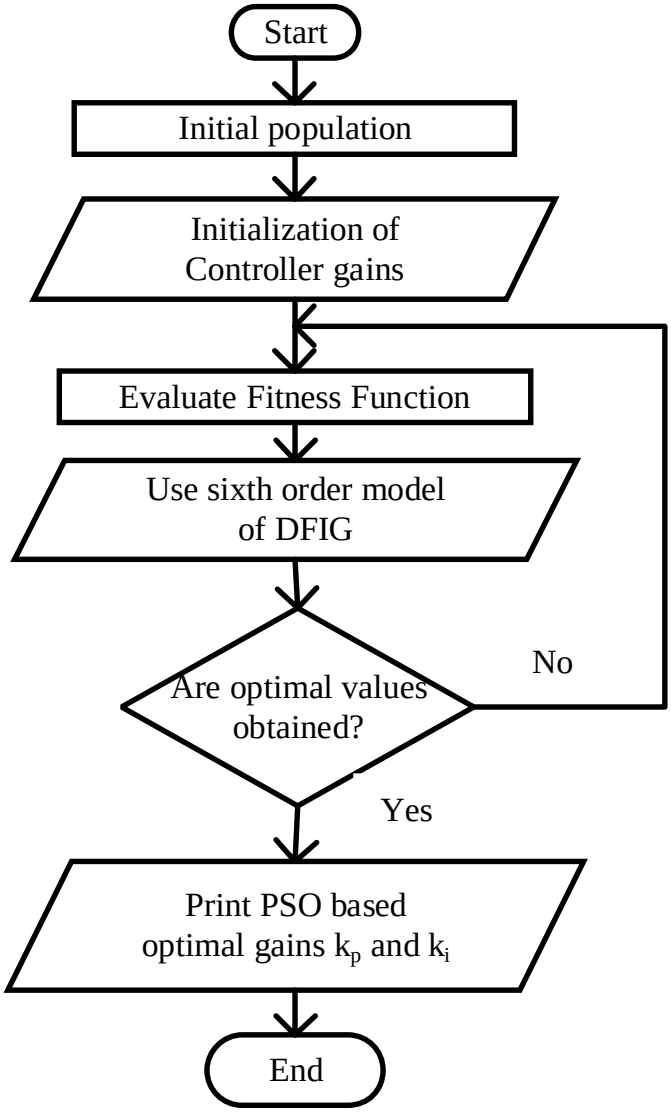


Figure 3.6: Algorithm for optimal $k_p$ and $k_i$ values.

### 3.4.2 Monte-Carlo Method

A high number of trials yields a good estimate of probability and, as a result, reliability. Therefore, a set of experiments must be conducted in a random order. Despite probability variations, the MC technique leads to the correct value as the number of trials grows. As a result, the MC technique is used in this work to calculate the likelihood of success and failure of the VSC interfaced with the DFIG-based WIPS system, as shown in Figure 1. Simulations have been conducted for various controller gain values while simultaneously analyzing the dc-link voltage of 1150V. In this work, the maximum value of dc-link voltage is obtained as 1261.4V without optimal gains. Thus, any value under 1150V+10% of 1150V (=1265V) is treated as expected

value. If dc-link voltage is within the expected value for a given value of gains, put a binary '1' otherwise '0'. Then, for the subsequent gain values, repeat step to get all the reliability-related functions. The gain values and corresponding dc-link voltage have been obtained, as illustrated in Table C.4 of Appendix.

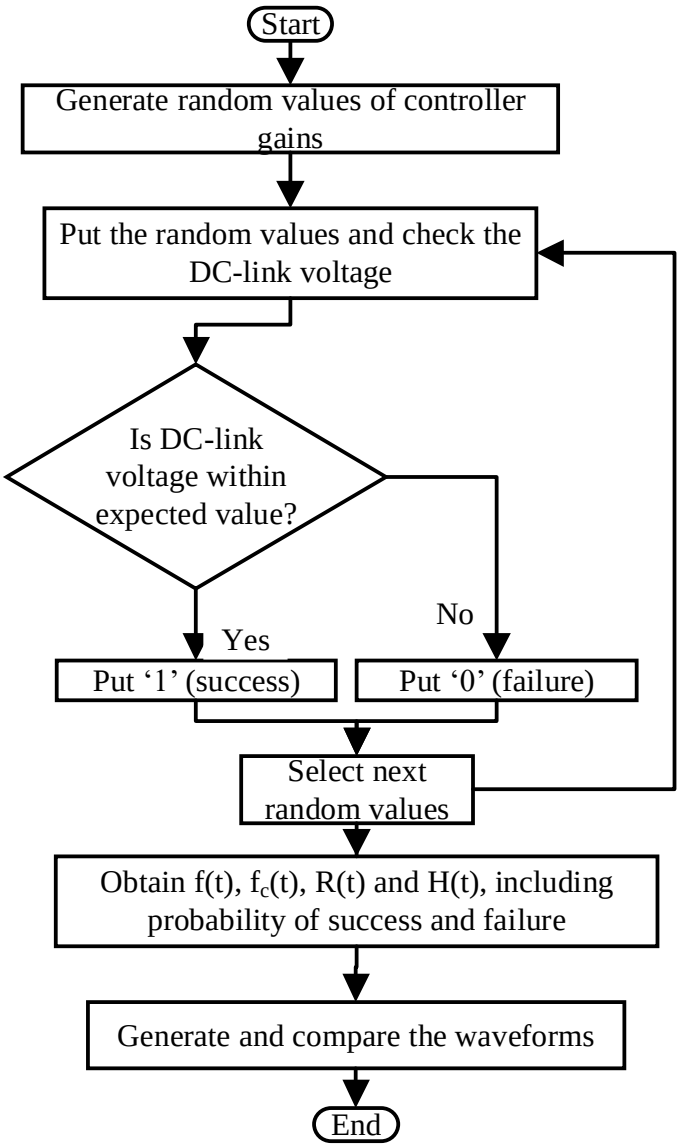


Figure 3.7: Monte-Carlo method for the reliability assessment.

The reliability-related indicators are assessed using direct analytic or stochastic techniques. So, to deal with the actual engineering problems, the stochastic simulation technique is suitable. Statistics or other basic calculations are employed in the analytical technique to access the indices. And the reliability indices are evaluated by simulation technique, which simulates the actual process and behaviour of the system. Monte-Carlo method estimates the probability

and reliability indices by simulating the outputs for several times.

The simulation technique, thus, deals with the problem as a set of a simulations performed within simulation interval. These simulation results show the following points.

- A number of simulations provide a better measure of the success probability and failure probability.
- The values of success and failure probabilities are obtained.
- The mean values of the probabilities are not a proper estimate of the real value.
- On the repetition of the process, the sequence outcomes provide a specific pattern of probability values.

Further, the analytical and simulation-based methods are used to evaluate reliability. The mathematical model is used to depict the analytical methods. For the computation of the reliability index, this model may be reduced to straight mathematical formulae. The MC approach, on the other hand, derives the reliability indices from the simulation process and the system's random behaviour. As a result, the MC technique approaches the issue as a series of real-world experiments carried out over a certain period of time. By counting event counts, the MC technique assesses the probability and reliability indices [198, 199].

## 3.5 Results and Discussion

The following steps are considered to accomplish this research work.
Step I: Verification of the DFIG's performance parameters with available literature.
Step II: Generation of natural LIV and Current waveforms considering IEEE Std 4-2013 standard.
Step III: Prepare and simulate the DFIG-based WECS model considering optimal gains obtained from proposed method viz. referred to Case 1.
Step IV: Apply 3-phase fault at grid terminals and simulate without (Case 2) and with (Case 3) PSO implementation.
Step V: Implement the impulse voltage generated in Step I at DFIG terminals and simulate without (Case 4) and with (Case 5) PSO implementation.
Step VI: Implement the Monte-Carlo method to determine the probability of VSC's success and

failure by examining the DC-link voltage at random $k_p$ and $k_i$ values.

Step VI: Draw the reliability indices function and compared with expected results.

Plot active power, reactive power, $V_{dc}$, and $\omega_r$ waveforms for Steps II, III, IV and analyze for expected results.

Table 3.2: Optimal gains obtained

| **Reference** | $k_p$ | $k_i$ | **Method** |
|---|---|---|---|
| [22] | 16.94 | 242.4 | GSA |
| **This Thesis** | **18** | **298** | **Proposed** |

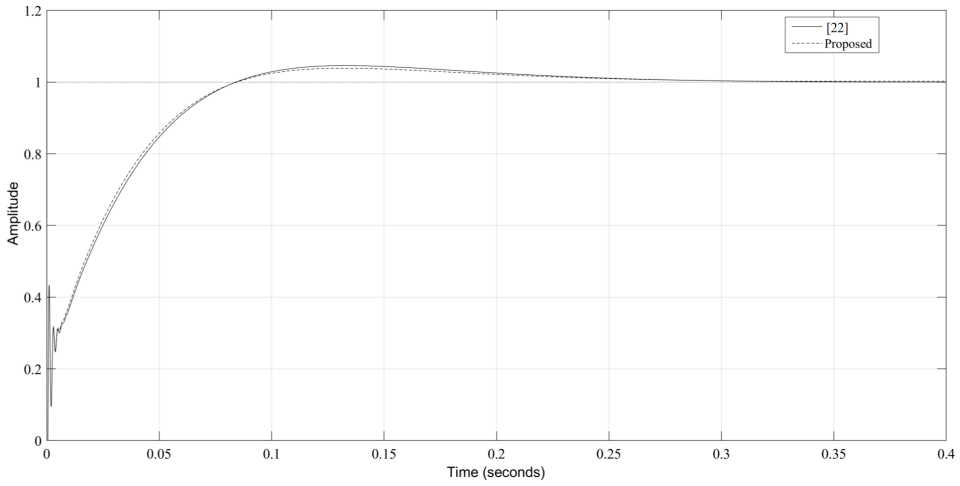


Figure 3.8: Comparison of Step response.

In the next subsections, chapter talks about output waveforms briefly. Implementing the PSO method yielded the $k_p$ and $k_i$ values of 18 and 298, respectively. Figure 3.8 illustrates a step response comparison, while Table 3.3 shows the response parameters. It has been shown that utilising the suggested approach yields a superior answer. The optimum gain values found in this chapter, as shown in Figures 3.9 - 3.12, improve the system's performance, as shown in Table 3.2. A Gravitational Search Algorithm is what GSA stands for.

Figure 3.9 shows how the active power may be raised using the proposed method, achieving the required amount of 9 MW. In addition, as illustrated in Figure 3.10, the reactive power tries to maintain its goal value of 0 MVar. Figures 3.11 and 3.12 show how the proposed method enables the other two performance criteria, DFIG rotor speed and DC link voltage, to reach their

desired values of 1.2 p.u. and 1150 V, respectively. When compared to existing literature, the optimal values discovered using the proposed method provide better step response parameters and performance characteristics for the test system used in this chapter.

Table 3.3: Step response parameters obtained

| Parameters | Reference [22] | Proposed |
|---|---|---|
| Rise Time(s) | 0.0584 | 0.0562 |
| Peak Time(s) | 0.1330 | 0.1321 |
| Settling Time(s) | 0.1970 | 0.1835 |
| %Peak Overshoot | 4.6206 | 3.8821 |
| Peak Amplitude | 1.0462 | 1.0388 |

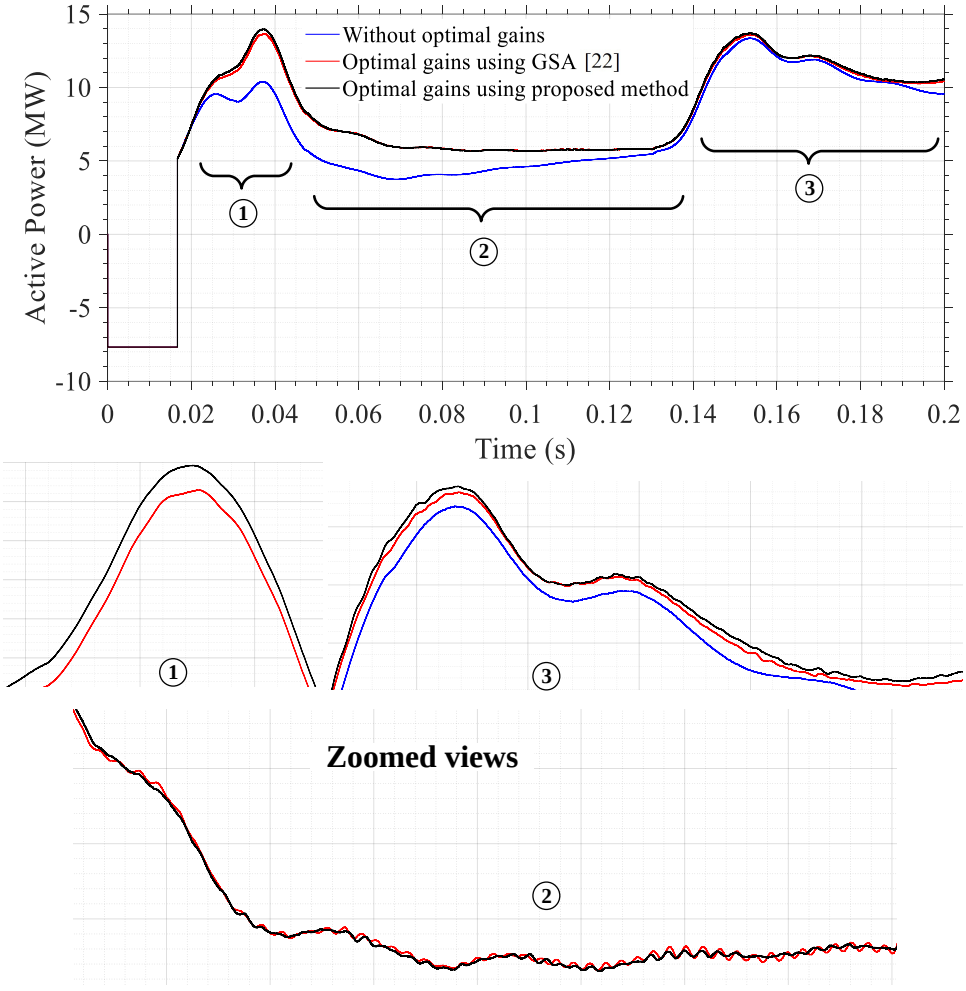


Figure 3.9: Real power comparative waveform.

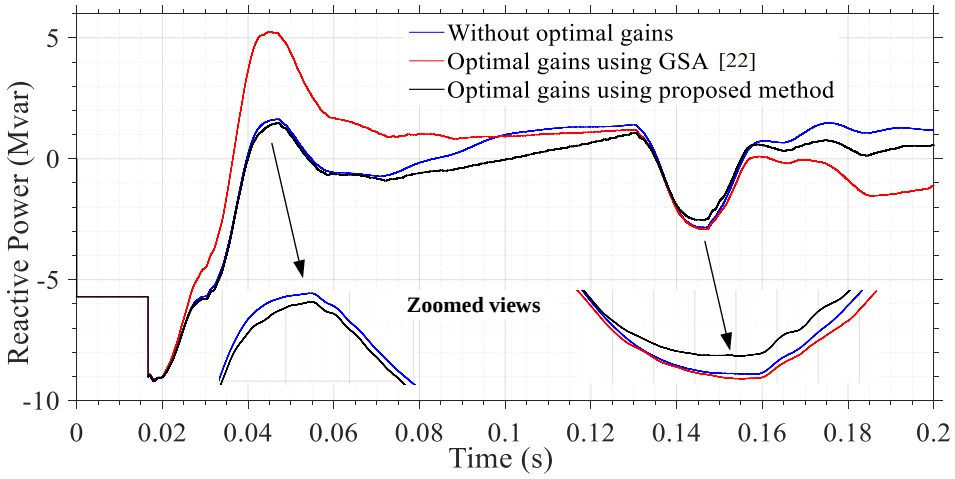


Figure 3.10: Reactive power comparative waveform.

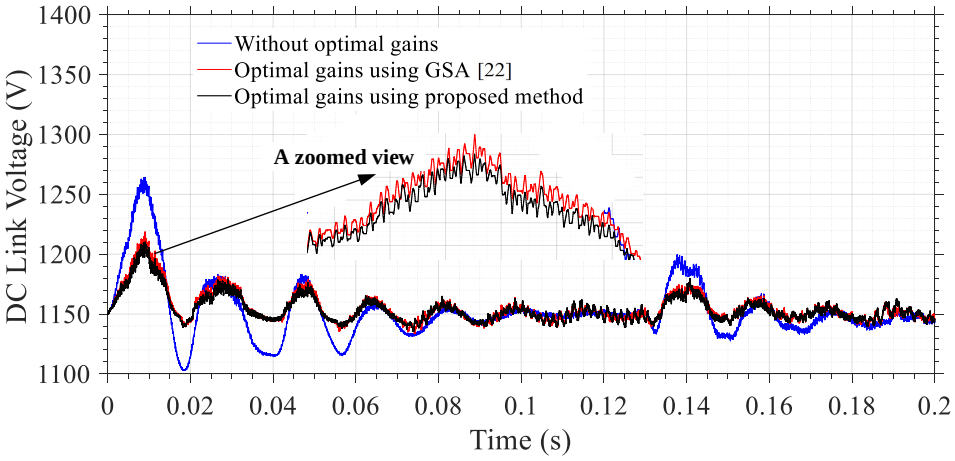


Figure 3.11: DC-link voltage comparative waveform.

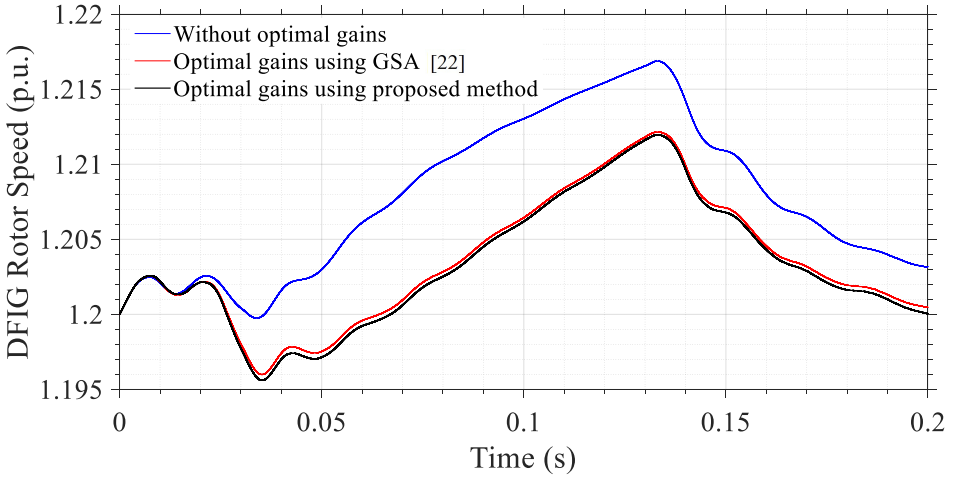


Figure 3.12: Rotor speed comparative waveform.

### 3.5.1 Impulse voltage and current generation

Figure 3.13a shows the impulse voltage waveform for the particular values of $R_f$, $L_f$, $R_t$, $L_t$, $C_l$, and $L_l$ for the impulse voltage generation circuit shown in Figure 3.3. It can be seen that the variation in any parameter(s) mentioned in Equations (3.7a) and (3.7b) results in a variation in the front time ($T_f$) as well as the tail time ($T_t$), which is summarised in Table 3.4.

Figure 3.13b shows the impulse current waveform for the specific values of $R$, $L$, $R_l$, and $L_l$ for the impulse current generation circuit in Figure 3.4. This waveform is generated for under-damped conditions, which can be illustrated by Equations (3.10) and (3.11). A minute increment in $R_f$ leads to an increment in $T_f$ and $T_t$ but shows a decrease in peak current, which is summarised in Table 3.4.

Figure 3.13c shows the rectangular pulse current waveform for a particular values of $L$ and $C$ for the rectangular pulse current generation circuit shown in Figure 3.5. Slight increment in $C$, decrease in $L$ and $R_l$ lead to an increment in $T_d$ and $T_t$ with increment in $I_p$ which is summarised in Table 3.4.

### 3.5.2 Fault analysis with and without optimal gains

This chapter looks at an DFIG-based WIPS, which consists of a wound rotor type induction generator and an AC-DC-AC IGBT-based converter. The stator is powered by a grid supply of 120 kV, 60 Hz, while the rotor is supplied by a VSC. A schematic representation is shown in Figure 3.2. Six 1.5 MW WTs were coupled to create a 9 MW WF, which is a satisfactory result. Limiting the reactive power produced by the WTGs to 0 MVar is also a desirable output. This WF is connected to a 25 kV distribution grid. This distribution system exports energy to the grid through a 30 km feeder. The wind speed is also adjusted at 15 m/s, and the torque controller is used to maintain the induction generator rotor speed at 1.2 pu (1440 rpm). Waveforms of system parameters $P$, $Q$, $Vdc$, and $\omega_r$ are generated for the five cases mentioned above. The explanation of all waveforms continues in this chapter.

Figure 3.14 describes the $P$ output waveform of a VSC-based DFIG system. The system produces 9 MW in the beginning. The positive sequence voltage drops suddenly, causing an oscillation on the DFIG output power at t=0.03 s. The output power becomes too small (nearly zero) during the 3-phase fault. The optimal values of gain parameters are obtained using PSO and observed that the power attains a value greater than zero during the fault, which is desirable.

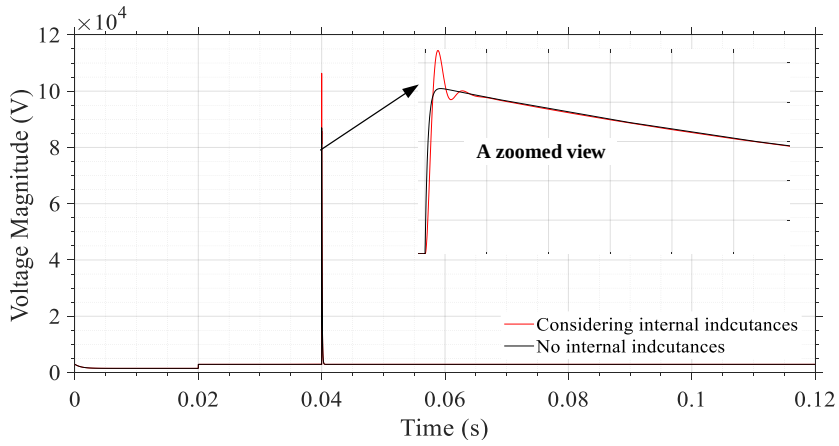


(a)

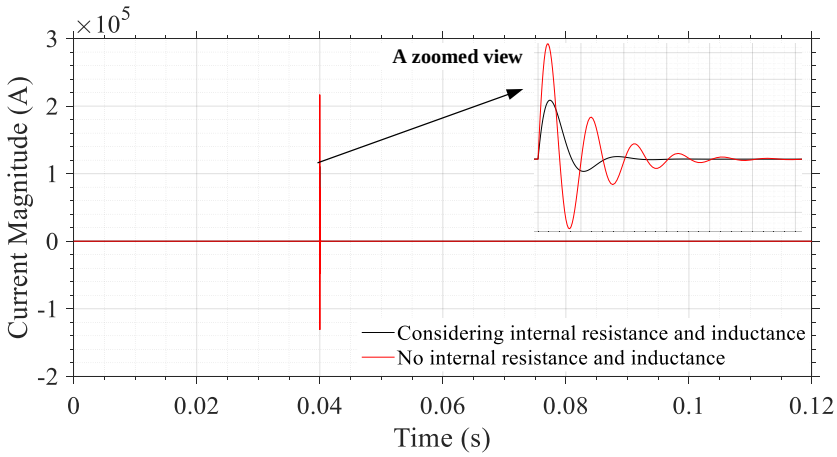


(b)

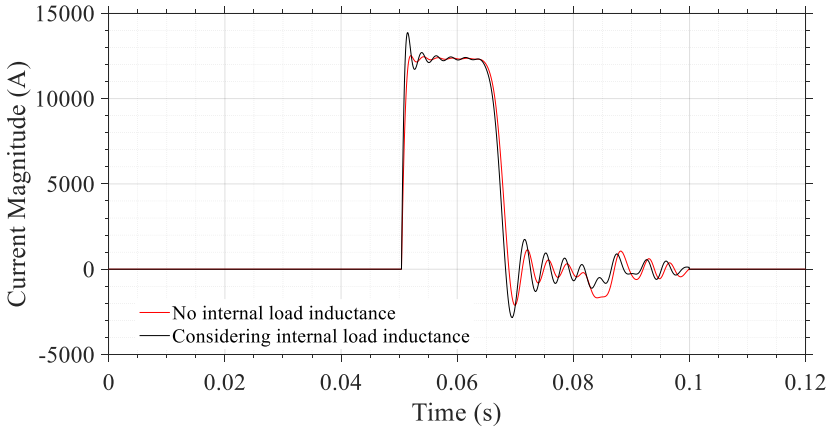


(c)

Figure 3.13: Waveforms generated for (a) Impulse voltage (b) Impulse current (c) Rectangular pulse current.

Table 3.4: Generation of standard LI waveforms by varying generator parameters

| **Impulse voltage with 100 kV charging voltage** | | | | | |
|---|---|---|---|---|---|
| $R_f(ohm)$ | $V_p(kV)$ | $T_f(\mu s)$ | $T_t(\mu s)$ | % error ($T_f$ and $T_t$) | $C_l(nF)$ |
| 100 | 97.19 | 1.14 | 50.00 | 5 and 0 | 1.0 |
| 105 | 97.12 | 1.25 | 50.13 | -4.16 and -0.26 | 1.5 |
| 112 | 97.03 | 1.28 | 50.14 | -6.66 and -0.28 | 2.0 |
| 115 | 97.00 | 1.34 | 50.17 | -11.66 and -0.34 | 2.5 |
| 120 | 96.92 | 1.42 | 53.34 | -18.33 and -6.68 | 3.0 |
| **Impulse current with 100 kV charging voltage** | | | | | |
| $R_f(ohm)$ | $I_p(kA)$ | $T_f(\mu s)$ | $T_t(\mu s)$ | % error ($T_f$ and $T_t$) | |
| 0.80 | 16.36 | 6.96 | 11.40 | -74 and 14 | |
| 0.85 | 14.45 | 6.22 | 11.57 | -55.5 and 15.7 | |
| 0.90 | 11.57 | 5.50 | 11.65 | -37.5 and 16.5 | |
| 0.95 | 10.60 | 5.30 | 11.82 | -32.5 and 18.2 | |
| 1.00 | 8.85 | 5.08 | 11.92 | -27 and 19.2 | |
| **Rectangular pulse current with 100kV charging voltage** | | | | | |
| $L(\mu H)$ | $C(\mu F)$ | $R_l(ohm)$ | $T_d$ (ms) | $T_t$ (ms) | $I_p(kA)$ |
| 0.63 | 99 | 8 | 15 | 17 | 1.846 |
| 0.48 | 132 | 6 | 15 | 17 | 2.366 |
| 0.32 | 198 | 4 | 15 | 18 | 3.312 |
| 0.16 | 396 | 2 | 15 | 34 | 5.514 |
| 0.04 | 1586 | 0.5 | 16 | 83 | 11 |

On the other hand, $P$ attains greater value in comparison to Cases 2 and 3 when an impulse fault is applied. This power is observed higher for Case 5, as described in Table 3.5.

Figure 3.15 describes $Q$ output waveform. It is expected that the $Q$ must be balanced and kept at 0 MVar. In normal operating condition, the $Q$ shows some negative value because in induction generators, the reactive power is required to establish the air gap magnetic flux. Therefore, in case of grid connection, it draws reactive power from the grid to maintain its air gap flux. The same concept is also applicable for the other cases. The value of $Q$ during

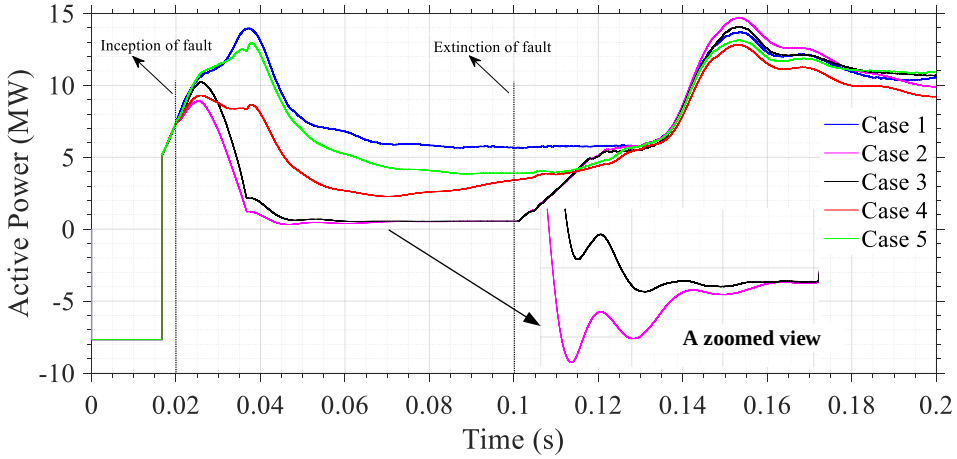


Figure 3.14: Real power during 3-phase and Impulse faults.

faults is greater in Cases 3 and 5 in comparison to Cases 2 and 4, respectively. It shows that using the PSO algorithm in obtaining the optimal gain values is favorable for the $Q$ value. The comparative analysis is performed and shown in Table 3.5.

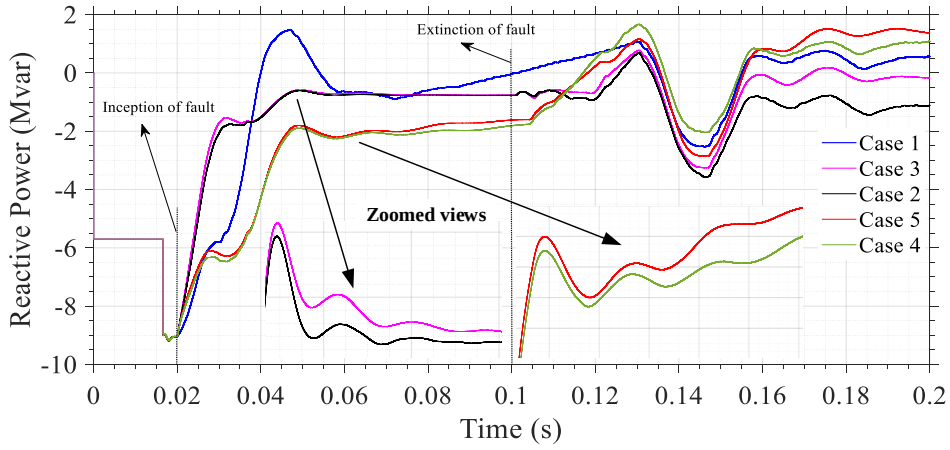


Figure 3.15: Reactive power during 3-phase and Impulse faults.

Figure 3.16 describes $V_{dc}$ output waveform of a VSC-based DFIG system. $V_{dc}$ has to be regulated at 1150 V. As it is seen that the $V_{dc}$ value tries to come closer to the desirable rated value in Cases 3 and 5 in comparison to the Cases 2 and 4, respectively and illustrated accordingly in Table 3.5. During the occurrence of fault, the grid voltage declines and thus, the grid side converter is unable to transmit the electrical power from rotor side converter to the grid. Therefore, the additional energy moves to charge the DC-link capacitor and thus, DC-link voltage rises rapidly.

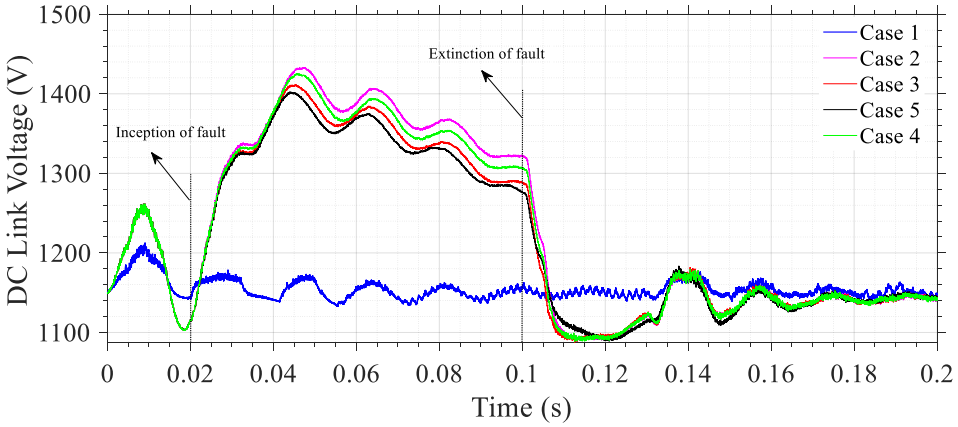


Figure 3.16: DC-link voltage during 3-phase and Impulse faults.

Figure 3.17 describes $\omega_r$ output waveform. In the model, the control system uses a torque controller in order to maintain the speed at 1.2 pu of synchronous generator speed. The value of $\omega_r$ is expected to be lesser in Cases 3 and 5 in comparison to Cases 2 and 4, respectively, as demonstrated in Table 3.5.

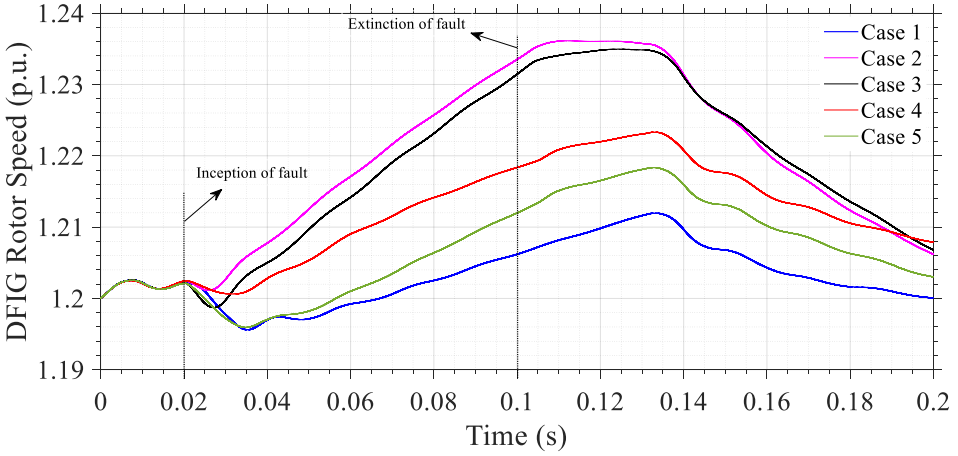


Figure 3.17: Rotor speed during 3-phase and Impulse faults.

The comparative statement provided in Table 3.5 can be summarized as follows, where Cases 2 to 5 have been considered mainly for a specified fault duration of 0.02 s to 0.1 s.

- Case 1: No faults have been assumed in normal condition, the expected real power ($P_1$) = 9 MW, reactive power ($Q_1$) = 0 MVar, DC link voltage ($V_{dc1}$) = 1150 V, and DFIG rotor speed ($\omega_{r1}$) = 1.2 pu.

- Case 2: The real power is lesser than the ($P_1$), negative reactive power is greater than the ($Q_1$), the DC link voltage is much greater than the $V_{dc1}$, and the rotor speed is greater in

Table 3.5: Comparative statement of all five cases

| Case | System parameters | | | |
|---|---|---|---|---|
| | $P$(MW) | $Q$(MVar) | $V_{dc}$ (V) | $\omega_r$ (pu) |
| Case 1 | $P_1$ | $Q_1$ | $V_{dc1}$ | $\omega_{r1}$ |
| Case 2 | $<$ Case 1 | negative VAr $>$ Case 1 | $>>$ Case 1 | $>$ all cases |
| Case 3 | (a) $<$ Case 1, (b) $>$ Case 2 | (a) negative VAr $>$ Case 1, (b) $<$ Case 2 | (a) $>$ Case 1, (b) $<$ Case 2 | (a) $<$ Case 2, (b) $>$ other cases |
| Case 4 | (a) $<$ Case 1, (b)$>$ Case 2, (c) $>$ Case 3 | negative VAr $>$ Case 1, 2 and 3 | (a) slight greater than Case 1, (b) $<$ Case 2, (c) $<$ Case 3 | (a) $<$ Case 2, (b) $<$ Case 3, (c) $>$ Case 1, (d) $>$ Case 5 |
| Case 5 | (a) $<$ Case 1, (b) $>$ other cases | (a) negative VAr $>$ Case 1, 2 and 3, (b) $<$ Case 4 | best in all cases | (a) $>$ Case 1, (b) $<$ other cases |
| Remark | Expect more real power to be delivered during faults | It must be as minimum as zero during faults | It is anticipated as close as the rated value during faults | It must be as same as rated during faults |

all cases.

- Case 3: In this case, the real power is lesser than the ($P_1$) but greater than Case 2, negative reactive power is greater than the ($Q_1$) but lesser than Case 2, the DC link voltage is much greater than the $V_{dc1}$ but lesser than Case 2, and the rotor speed is greater for Cases 1, 3, 4, and 5 but lesser than Case 2.

- Case 4: The real power is lesser than the ($P_1$) but greater for Cases 2 and 3, negative reactive power is greater than the ($Q_1$) and Cases 2 and 3, the DC link voltage is greater than the $V_{dc1}$ but lesser than Cases 2 and 3, and the rotor speed is greater than ($\omega_{r1}$) and Case 5 but lesser for Cases 2 and 3.

- Case 5: In this case, the real power is lesser than the ($P_1$) but greater for rest cases, negative reactive power is greater than the ($Q_1$) and Cases 2 and 3 but lesser than Case 4, the DC link voltage is best in Cases 2 to 4, and the rotor speed is greater than ($\omega_{r1}$) and lesser for the rest of the cases.

### 3.5.3 Reliability Assessment

The Monte-Carlo simulation method is implemented to assess the reliability of the adapted test system.[3] The reliability assessment of DFIG-based WIPS is shown using the creation of the distribution function. The appropriate probability of success and failure for randomly generated

[3]Sachin Kumar, Kumari Sarita, R.K. Saket, Dharmendra Kumar Dheer, R.C. Bansal, Saad Mekhilef, "Reliability Assessment for DFIG-based WECS Considering the Impact of 3-phase Fault and Lightning Impulse Voltage", International Transactions on Electrical Energy Systems, Wiley, pp. 1-19 (2021) doi: https://doi.org/10.1002/2050-7038.12952

gain parameter values ($k_p$ and $k_i$) of DFIG is determined via simulation. Simulations are conducted for various controller gain values while simultaneously analyzing the dc-link voltage of 1150V. The maximum value of dc-link voltage is obtained as 1261.4V without optimal gains. Thus, any value under 1150V+10% of 1150V (=1265V) is treated as expected value. If dc-link voltage is within the expected value for a given value of gains, put a binary '1' otherwise '0' [200]. Then, for the subsequent gain values, repeat step to get all the reliability-related functions. The gain values and corresponding dc-link voltage have been obtained and illustrated in Table C.4 of Appendix.

The binary output '1' and '0' signify the 'success' and 'failure' of a particular simulation performed. Further, these binary outputs of success and failure have been implemented to obtain the probability of success and probability of failure, as illustrated below.
In first simulation for gain values of 25 and 21 (Table C.4), the dc-link voltage is obtained within expected value of 1265V. Then, this simulation is considered as success (denoted with '1') and same has achieved for second simulation.

Next, for third and fourth simulations with gain values 47 & 58 and 49 & 49, respectively, the dc-link voltage is not obtained within expected value. Thus, these simulations are considered as failure (denoted with '0'). Likewise, other simulations give binary outputs for different gain values, as provided in Table 3.6 and computed as follows.

**Calculation of probability of success and failure:-**

$$\text{Probability} = \frac{\text{number of favourable outcome}}{\text{Total number of events}} \tag{3.17}$$

For first simulation–

$$\text{Probability of success} = \frac{1}{1} = 1 \tag{3.18}$$

$$\text{Probability of failure} = \frac{0}{1} = 0 \tag{3.19}$$

For second simulation–

$$\text{Probability of success} = \frac{2}{2} = 1 \tag{3.20}$$

$$\text{Probability of failure} = \frac{0}{2} = 0 \tag{3.21}$$

For third simulation–

$$\text{Probability of success} = \frac{2}{3} = 0.667 \tag{3.22}$$

$$\text{Probability of failure} = \frac{1}{3} = 0.333 \tag{3.23}$$

For fourth simulation–

$$\text{Probability of success} = \frac{2}{4} = 0.5 \tag{3.24}$$

$$\text{Probability of failure} = \frac{2}{4} = 0.5 \tag{3.25}$$

For fifth simulation–

$$\text{Probability of success} = \frac{3}{5} = 0.6 \tag{3.26}$$

$$\text{Probability of failure} = \frac{2}{5} = 0.4 \tag{3.27}$$

For sixth simulation–

$$\text{Probability of success} = \frac{3}{6} = 0.5 \tag{3.28}$$

$$\text{Probability of failure} = \frac{3}{6} = 0.5 \tag{3.29}$$

For seventh simulation–

$$\text{Probability of success} = \frac{4}{7} = 0.571 \tag{3.30}$$

$$\text{Probability of failure} = \frac{3}{7} = 0.429 \tag{3.31}$$

For last simulation–

$$\text{Probability of success} = \frac{62}{100} = 0.62 \tag{3.32}$$

$$\text{Probability of failure} = \frac{38}{100} = 0.38 \tag{3.33}$$

Further, with the help of Table 3.6, probability of success and failure are drawn as Fig. 3.18.

Table 3.6: Reliability assessment using Monte-Carlo method

| **No. of Simulation** | **Simulation Outcome** | **Binary output** | **Probability of** | |
|---|---|---|---|---|
| | | | **Success (Y)** | **Failure (N)** |
| 1 | Y | 1 | 1 | 0 |
| 2 | Y | 1 | 1 | 0 |
| 3 | N | 0 | 0.667 | 0.333 |
| 4 | N | 0 | 0.5 | 0.5 |
| 5 | Y | 1 | 0.6 | 0.4 |
| 6 | N | 0 | 0.5 | 0.5 |
| 7 | Y | 1 | 0.571 | 0.429 |
| 8 | N | 0 | 0.5 | 0.5 |
| 9 | N | 0 | 0.444 | 0.556 |
| 10 | N | 0 | 0.4 | 0.6 |
| — | — | — | — | — |
| — | — | — | — | — |
| — | — | — | — | — |
| — | — | — | — | — |
| 99 | Y | 1 | 0.626 | 0.374 |
| 100 | N | 0 | 0.62 | 0.38 |

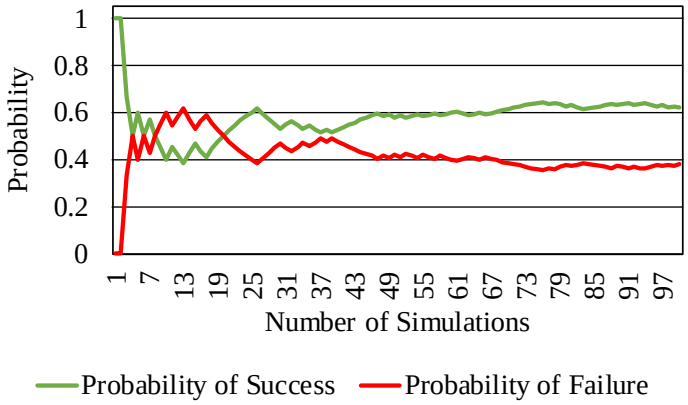


Figure 3.18: Probability of Success and Failure

Using Table 3.6, sets of simulations have been depicted, as mentioned in Table 3.7. Time

Table 3.7: Determination of reliability related functions

| **Simulation interval (in days)** | **Failures** | **Cumulative failures** | **Simulation with failures** | $f(t)$ | $f_c(t)$ | $R(t)$ | $H(t)$ |
|---|---|---|---|---|---|---|---|
| 0 | 6 | 0 | 38 | 0.157 | 0 | 1 | 0.157 |
| 1 | 4 | 6 | 32 | 0.105 | 0.157 | 0.842 | 0.125 |
| 2 | 4 | 10 | 28 | 0.105 | 0.263 | 0.736 | 0.142 |
| 3 | 5 | 14 | 24 | 0.131 | 0.368 | 0.631 | 0.208 |
| 4 | 2 | 19 | 19 | 0.052 | 0.5 | 0.5 | 0.105 |
| 5 | 3 | 21 | 17 | 0.078 | 0.552 | 0.447 | 0.176 |
| 6 | 3 | 24 | 14 | 0.078 | 0.631 | 0.368 | 0.214 |
| 7 | 3 | 27 | 11 | 0.078 | 0.710 | 0.289 | 0.272 |
| 8 | 3 | 30 | 8 | 0.078 | 0.789 | 0.210 | 0.375 |
| 9 | 5 | 33 | 5 | 0.131 | 0.868 | 0.131 | 1 |
| | | 38 | | | | | |

during which a set of simulations are performed, is being referred as simulation interval (in days). There are ten intervals in which ten simulations are performed in each interval. Then, number of failures, number of cumulative failures, number of simulations without failure have been calculated as follows.

$$f(t) = \frac{\text{Number of failures during an interval}}{\text{Total number of failures(=38)}} \tag{3.34}$$

f(t) calculated for ten intervals; $\frac{6}{38}$ (=0.157), $\frac{4}{38}$ (=0.105), $\frac{4}{38}$(=0.105), $\frac{5}{38}$(=0.131), ....., $\frac{5}{38}$(=0.131).

$$f_c(t) = \frac{\text{Cumulative number of failures during an interval}}{\text{Total number of failures(=38)}} \tag{3.35}$$

$f_c(t)$ calculated for ten intervals; $\frac{0}{38}$ (=0), $\frac{6}{38}$ (=0.157), $\frac{10}{38}$ (=0.263), $\frac{14}{38}$ (=0.368), ....., $\frac{33}{38}$ (=0.868).

$$R(t) = \frac{\text{Cumulative number of survivors (simulation without failure) during an interval}}{\text{Total number of failures(=38)}} \tag{3.36}$$

$R(t)$ calculated for ten intervals; $\frac{38}{38}$ (=1), $\frac{32}{38}$ (=0.842), $\frac{28}{38}$ (=0.736), $\frac{24}{38}$ (=0.631), ....., $\frac{5}{38}$ (=0.131).

$$H(t) = \frac{f(t)}{R(t)} \tag{3.37}$$

$H(t)$ calculated for ten intervals; $\frac{0.157}{1}$ (=0.157), $\frac{0.105}{0.842}$ (=0.125), $\frac{0.105}{0.736}$ (=0.142), $\frac{0.131}{0.631}$ (=0.208), ....., $\frac{0.131}{0.131}$ (=1).

Implementing the above simulation results, the reliability assessment is performed by evaluating the reliability or survival function ($R(t)$), cumulative distribution function ($f_c(t)$), failure density function ($f(t)$), and hazard rate function ($H(t)$), as described by Equations (1.3)–(1.4). The method for representing failure probability of a component is its reliability, viz. the probability that the system or equipment would not fail within time interval (0, t).

Following steps are employed for the reliability assessment.

- Compute the overall number of failures in each time spell
- Evaluate the reliability indices $R(t)$, $f_c(t)$, $f(t)$ and $H(t)$ [1, 201].

All functions are explained graphically in Figures 3.19a - 3.19c, respectively. The results obtained are reproduced in Table 3.7, which is described as follows.

- Ten number of simulations are chosen as one interval.
- Number of failures are examined via simulation.
- Cumulative failures are the summation of failures in each interval.
- Obtain the number of simulation with failures on the next interval, which is equal to the total cumulative failures (i.e. 38) minus the cumulative failures occurred in that time interval.

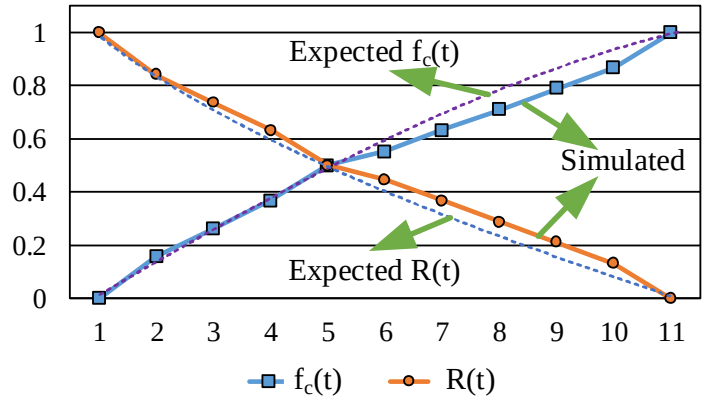


(a)

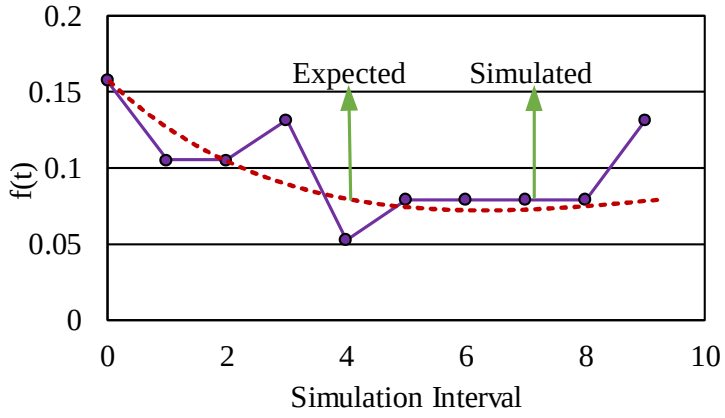


(b)

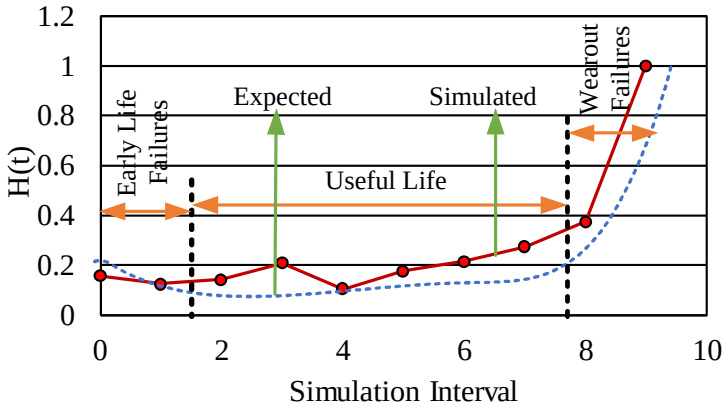


(c)

Figure 3.19: Generated functions for (a) Cumulative distribution and Reliability (b) Failure density (c) Hazard Rate.

- $f(t)$ = (number of failures during an interval) / 38.
- $f_c(t)$ = (cumulative number of failures) / 38.
- $R(t)$ = (cumulative number of survivors) / 38.

- $H(t) = \frac{f(t)}{R(t)}$.

## 3.6 Summary

The test system considered in this chapter was used to conduct the reliability assessment. Three different kinds of lightning waveforms were created using actual equivalent circuits and compared to regular circuits. The system is next tested for performance and reliability by exposing it to lightning and three-phase faults. The six-order transfer function of DFIG has also been used to evaluate the system's performance. It was discovered that adjusting the gain settings enhanced the test system's performance. The findings were then compared to [22] and it was discovered that the WIPS's performance had improved.

Furthermore, the waveforms were compared under the following situations to assess the system's performance and determined to be superior.

- Without any fault and optimized gain values
- With three-phase fault and no optimized gain values
- With three-phase fault and optimized gain values
- With Lightning Impulse fault and no optimized gain values
- With Lightning Impulse fault and optimized gain values

Furthermore, the reliability assessment was carried out using the Monte-Carlo simulation technique, and different reliability indices were computed, including the reliability function, cumulative distribution function, failure distribution function, and hazard rate function. The reliability indices functions revealed that the VSC system may fail and that reliability could be reduced at specific simulation periods. Finally, it was shown that by decreasing the amount of failures in the converter during lightning faults, the case system's reliability may be enhanced.

The following chapter discusses the reliability of an IEEE 33 bus system that is combined with Wind-Solar-Battery. It has been discovered that using energy sources with optimum placements and ratings improves the test system's reliability.